SCIENCE CHINA
Technological Sciences

October 2012 Vol.55 No.10: 2941–2952
doi: 10.1007/s11431-012-4952-0

Hybrid undulatory kinematics of a robotic Mackerel (*Scomber scombrus*): Theoretical modeling and experimental investigation

WEN Li[1,2*], WANG TianMiao[2], WU GuanHao[3] & LIANG JianHong[2]

[1] *Museum of Comparative Zoology, Harvard University, 26 Oxford Street, Cambridge, MA 02138, USA;*
[2] *Robotic Institute in School of Mechanical Engineering and Automation, Beihang University, Beijing 100191, China;*
[3] *State Key Laboratory of Precision Measurement Technology and Instruments, Department of Precision Instruments, Tsinghua University, Beijing 100084, China*

Received October 1, 2011; accepted March 30, 2012; published online June 23, 2012

Fishes that use undulatory locomotion occasionally change their inherent kinematics in terms of some natural behavior. This special locomotion pattern was vividly dubbed "hybrid kinematics" by biologists recently. In this paper, we employed a physical model with body shape of a Mackerel (*Scomber scombrus*), to use the three most typical undulatory kinematics: anguilliform, carangiform and thunniform, to investigate the hydrodynamic performance of the so-called "hybrid kinematics" biological issue. Theoretical models of both kinematics and hydrodynamics of the physical model swimming were developed. Base on this model, the instantaneous force produced by fish undulatory body and flapping tail were calculated separately. We also quantitatively measured the hydrodynamic variables of the robotic model swimming with the three undulatory kinematics on an experimental apparatus. The results of both theoretical model and experiment showed that the robot with thunniform kinematics not only reaches a higher speed but also is more efficient during steady swimming mode. However, anguilliform kinematics won the speed race during the initial acceleration. Additionally, the digital particle image velocimetry (DPIV) results showed some difference of the wake flow generated by the robotic swimmer among the three undulatory kinematics. Our findings may possibly shed light on the motion control of a biomimetic robotic fish and provide certain evidence of why the "hybrid kinematics" exists within the typical undulatory locomotion patterns.

hybrid kinematics, robotic fish, digital partial image velocimetry (DPIV), self-propulsive

Citation: Wen L, Wang T M, Wu G H, et al. Hybrid undulatory kinematics of a robotic Mackerel (*Scomber scombrus*): Theoretical modeling and experimental investigation. Sci China Tech Sci, 2012, 55: 2941–2952, doi: 10.1007/s11431-012-4952-0

1 Introduction

The most enduring features of many literatures on undulatory locomotion of live fish is the classification of swimming mode into general "pattern" based on species. Considering the movement patterns, eels, mackerels, and tunas, which are termed anguilliform, carangiform, and thunniform swimmers, are the three most typical types of body caudal fin (BCF) fish [1]. Conventionally, each of the species has inherent motion, for instance, a live mackerel (*Scomber scombrus*) is usually considered to swim using the carangiform kinematics, but not the anguilliform or the thunniform kinematics. Nevertheless, fishes that use all the three types of kinematics swim to escape predators, to feed, and migrate to find mates, good thrust performance in each above behavior is necessary [2], and are critical to survival. As an example, leopard sharks is defined as carangiform species, but are observed to swim in an anguilliform pattern from time to time. Needlefish have slender anguilliform bodies, but occasionally use the carangiform swimming

*Corresponding author (email: liwen@oeb.harvard.edu)

pattern [3]. Moreover, the eels ware observed to use less body movement during steady swimming just like a mackerel [4], rather than a whole body wave that was documented by Lighthill [5]. These special locomotion phenomena were vividly dubbed "hybrid kinematics" by the biologists recently [3]. Do such fish swimming kinematics have any scientific significance? To date, systematic studies on this issue have not yet been performed.

Besides the above descriptions of the "hybrid kinematics" in live fish, the inspiration from biological hybrid kinematics may also possibly shed light on the biomimetic underwater vehicle [6–14]. Recall that the biomimetic robots were usually programmed to move following the biological kinematics data that were directly obtained from live fish data. For instance, Hultmark [15] investigated the hydrodynamic performance of an anguilliform robotic swimmer using kinetic parameters obtained from the American eels 4. The kinematics data of Yu et al.'s [9] robotic carangiform fish were obtained from biological results of the mackerels [16]. The robotic thunniform swimmer designed by Barrett [17] and Anderson et al. [18] used the kinematics data from the live yellow-fin tuna [19]. Note that the natural selection is surely resulting in the optimal thrust performance [2]. Likewise, if a robotic mackerel was merely programmed to using the carangiform locomotion, would this possibly lead to an unconvinced thrust performance?

In this paper, we aim to investigate the hybrid kinematics propulsion by using both theoretical and experimental approaches. More specifically, we implemented a biomimetic robotic fish and programmed it with three most typical undulatory fish kinematics: Anguilliform, carangiform and thunniform kinematics. Understanding how the kinematics of a live or robotic fish affects its thrust performance requires knowledge and data of the hydrodynamics. Experimental apparatus was implemented for obtaining quantitative hydrodynamic variables of the robotic fish under self-propulsive condition. A theoretical model was developed to calculate the instantaneous force of both the undulating body and the flapping caudal fin. The high-resolution digital particle image velocimetry (DPIV) techniques [20–22] were used to quantify the time-averaged thrust force generated by the robotic swimmer. By combining experimental and theoretical analysis, we obtained the self-propulsive speed, instantaneous force, power consumption, wake flow field and thrust efficiency of the robotic fish. Finally, we will discuss the results to elucidate several interesting hydrodynamic aspects of the "hybrid kinematics".

2 Modeling of hybrid undulatory kinematics

How do we mathematically distinguish the three distinct undulatory movement patterns? Early biological studies suggested that the body wavelength during steady swimming and the percentage of the body that undergoes undulatory movement are the major preliminary criteria that distinguishes the BCF locomotion [23]. According to the study of Eric Tytell's study [4], body undulation in anguilliform swimmers is almost over the whole length. Given that the anterior of the robotic swimmers' body (roughly 30% of its total body length) is mechanically rigid, the lateral movement for anguilliform kinematics starts from $0.3L$ measured from the nose of the robotic fish. Dickson et al. [24] proposed that undulatory body movement occurs at (35%–40%)L in mackerels and tunas. Therefore, in the present study, the body movement for carangiform and thunniform kinematics starts from $0.35L$ measured from the nose of the robotic fish. The wavelength of typical anguilliform kinematics is set to $0.642L$ 4. For carangiform swimmers, the wavelength is set to $0.95L$, which is consistent with the mean propulsive wavelength of live mackerels as reported by Hess and Videler [16]. Finally, the wavelength (λ=1.25L) of the yellow-fin tuna (*Thunnus albacares*) reported by Dewar et al. [19] is used for thunniform kinematics. Figure 1 shows the schematics of one instance when the three undulatory kinematics are imposed on the robotic mackerel's body.

The caudal fin movement of anguilliform kinematics forms the angle tangent to the body wave at the point of conjunction [5]; also see Figure 1(a) for notation. However, Lauder et al. [25] demonstrated that the caudal fin movement of most *scombrid* fish (e.g. the mackerels and tunas) do not simply function as a tangent extension of the body wave, but behave as a distinct propeller like an oscillating foil with adjustable pitch angle θ_c, as can be seen from Figure 1(b). In this paper, the pitch angle of the caudal fin is described as the angle between the line from the leading edge to the trailing edge of the artificial tail and the free stream flow (in the forward axial direction). On the basis of the X-ray scan results of intervertebral bending angles of chub mackerel and Kawakawa tunas by Dickson et al. [24], the pitch angles are 20.5° and 11.5° for carangiform and thunniform kinematics, respectively, while a pitch angle of 26.5° is employed for anguillform kinematics [5]. The above description accounts for a quantitative characterization and a clear separation between the three distinct BCF kinematics.

The above description accounts for a quantitative characterization and a clear separation between the three undulatory kinematics. To construct the mathematical model of hybrid kinematics, we conceptualized undulating swimming of robotic fish as the movement of a waving body and an independent oscillating foil [16]. The kinematics of the undulating body takes the following form [5]:

$$h(x,t) = (c_1 x + c_2 x^2)\sin[kx \pm \omega t], 0 < x < 2L/3 - c. \quad (1)$$

See Figure 1(a) for notation, $h(x,t)$ denotes the displacement along the lateral direction in a body-fixed coordinate system, with x measured from $1/3L$ of the robotic fish, where L represents the total length of the robotic mackerel's body. c denotes the chord length of caudal fin; $k=2\pi/\lambda$

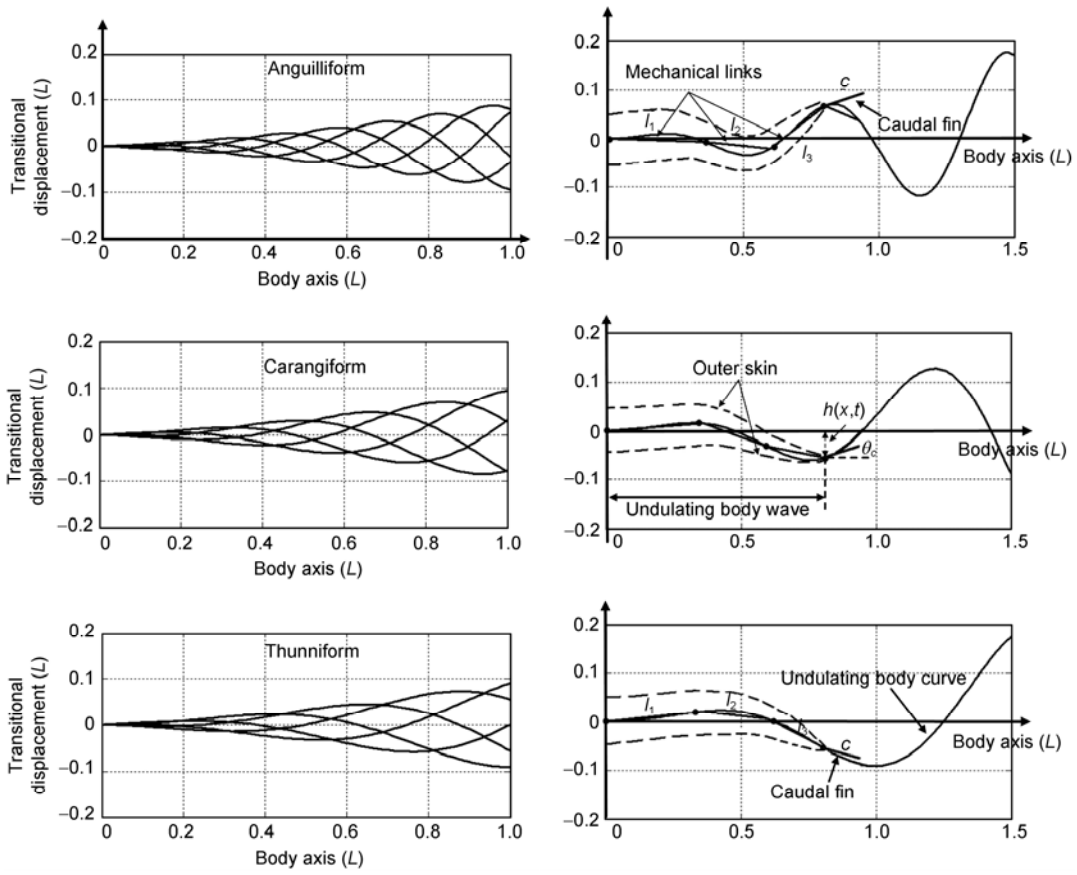

Figure 1 Schematics of the robotic Mackerel and the mechanical links that are used to fit the curves of the fish kinematics of (a) anguilliform, (b) carangiform and (c) thunniform.

denotes the wave number, which corresponds to body wavelength λ; ω denotes the circular frequency of oscillation and $\omega=2\pi f$; and c_1, and c_2 are applied and adjusted to achieve a specific value for the amplitude envelope of the body. The heave and pitch motions of the oscillating tail at the caudal fin center of mass point can be defined as [26]

$$\begin{cases} h_c = [h(x,t)]_{x=L-2c/3}, \\ \theta_c = \theta_{\max} \sin\left[\dfrac{2\pi}{\lambda}x \pm 2\pi ft + \psi\right]_{x=L-2c/3}, \end{cases} \tag{2}$$

where h_c and θ_c denote the heave and pitch motions, respectively; c denotes the chord length of the caudal fin; f represents the oscillating frequency; ψ is the phase angle between the heave and the pitch motions; $x=L-2c/3$ denotes the position of the caudal fin center of mass, which connects the caudal peduncle. $\theta_{\max}$ represents the pitch angle amplitude of the caudal fin. Therefore, $\theta_{\max}$ =26.5°, 20.5° and 11.5° are for anguilliform, carangiform and thunniform kinematics, respectively. Moreover, all three kinematics have the same maximum displacement at the tail fin end (h=0.1L), which is in accordance with the observed results of the live counterparts [4, 16].

3 Theoretical modeling of hydrodynamics

3.1 General description of the theoretical model

This part introduces the hydrodynamic model that takes the undulatory kinematics as the input and returns important thrust performance parameters. More specifically, this model can be used to calculate the instantaneous force of undulating body and oscillating caudal fin. As shown in Figure 2, the forces generated by each part of the robotic fish, i.e., rigid head, undulating body, and oscillating tail, were calculated as the sum of skin friction, form force, and reactive force, respectively. The present undulating body dynamic model combines two classical theories: large-amplitude elongated-body theory (LAEBT), which focuses on the reactive force without considering the form and skin friction [5], and the resistive model theories, which mainly consider form force and skin friction without taking into account the reactive effect [27]. Furthermore, the caudal fin was treated as a rigid extension of the body wave, and was modeled by integrating the quasi-steady lift force [28] and the added mass fluid force [5]. In the present model, we only consider the axial direction of fish swimming with lateral and rotational direction constraints.

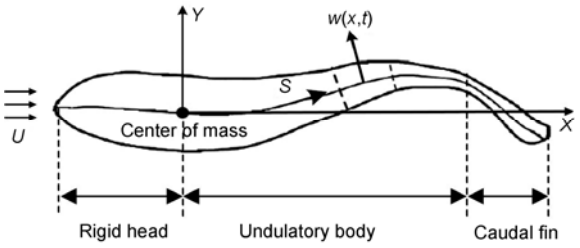

Figure 2 Dorsal sketch of an undulating fish swimming at a self-propelled speed U in x and y global coordinates, where o indicates the fish center of mass, and symbol S denotes the midline along the fish body. Note that the anterior one-third part is aligned with the flow direction.

3.2 Rigid head force

In general, the total force acting on the anterior rigid head of the robotic fish takes the form:

$$F_h = F_{sh} + F_{fh} + F_{ah}, \tag{3}$$

where F_{sh} and F_{fh} denote the skin force and form force, respectively; F_{ah} denotes the reactive force of the rigid head. The form force is produced by differences in pressure on the surface of an object, which varies with the square of swimming velocity U [28]:

$$F_{fh} = -0.5\rho U^2 C_{fh} A_h, \tag{4}$$

where A_h denotes the projected area at cross section plane of the fish head, and C_{fh} denotes the form force coefficient, which derives from the form force coefficient on a cone sphere [28]:

$$C_{fh} = \frac{6}{1+\sqrt{Re}_h} + 0.4. \tag{5}$$

Re_h is calculated by $Re_h = L_h U/v$, with the length of the rigid head as the characteristic length, and L_h denotes the length of the rigid head, and $L_h = (1/3)\ L.\ v$ denotes the kinematics viscosity of fluid, and $v = 10^{-6}$. The skin force is generated by the resistance of the fluid shear effect, which increases in proportion to the speed of flow [28]:

$$F_{sh} = -0.5\rho C_{sh} S_h U. \tag{6}$$

S_h denotes the wetted surface area of the head. The skin force coefficient C_{fh} is defined as a function of local axial Reynolds number in a turbulent flow:

$$C_{sh} = 0.059 \,|\, Re_h^{0.2} \,|. \tag{7}$$

The parameter in (7) is fitted by the experimental data of a flat plate reviewed by Hoerner [28].

3.3 Undulatory body force

Both the form and viscous force of the undulating body were calculated by the resistive model [27]. By using undulated kinematics that is normal and tangential to the body midline and by integrating force from the head to the caudal peduncle, the undulating body's form force in the axial direction along the x axis can be obtained as

$$F_{fb} = \frac{1}{2}\rho \int_0^{L-c} [(C_{fb} s(x) v_{x\perp}{}^2) \sin\theta \mathrm{d}x, \tag{8}$$

where $v_{x\perp} = \partial h(x,t)/\partial t$, which denotes the velocity of body undulation normal to the body midline; $s(x)$ represents the local depth of whole robotic fish and will be introduced later in eq. (25); $\theta = \partial h(x,t)/\partial x$, which denotes the angle of the local body segment in the axial direction along the x axis; the form body force coefficient C_{fb} is determined by empirical description of turbulent flow normal to the cylinder with ellipse cross-section [28]:

$$C_{fb} = 1.2 + 4Re_{x\perp}{}^{-0.5},\ Re_{x\perp} = s(x) v_{x\perp}/\upsilon. \tag{9}$$

The skin force of the undulating body along x axis can be calculated by the following:

$$F_{sb} = \frac{1}{2}\rho \int_0^{L-c} (C_{x\|} s(x) v_{x\|}{}^2) \cos\theta \mathrm{d}x, \tag{10}$$

where the body skin force coefficients $C_{x\|}$ is determined by empirical description of turbulent flow parallel to a flat plate [28] and is defined as

$$C_{sb} = 0.37(\log Re_{x\|})^{-2.6},\ Re_{x\|} = x v_{x\|}/\upsilon, \tag{11}$$

where $v_{x\|} = \dfrac{\partial w(x,t)}{\partial x}$, which denotes the body wave velocity that is tangential to the body midline. It should be note that the parameters in both (9) and (11) were fitted by the experimental data reported by Hoerner [28]. The acceleration reactive force generated by the undulating body is calculated using the large-amplitude elongated body theory (LAEBT) [5]. As shown in Figure 2, for a continuous undulating body with self-propulsive swimming speed U, the body waving speed $w(x,t)$ is

$$w(x,t) = \frac{\partial h(x,t)}{\partial t} + U(t)\frac{\partial h(x,t)}{\partial x}. \tag{12}$$

As the carangiform fish body is relatively elongated and its cross-section area changes gently along the axial direction [16], we apply the LAEBT to the fish body reaction force in the axial direction. Therefore, the force due to the fluid-added mass effect is as follows:

$$F_{ab} = [m_a w(\frac{\partial h}{\partial t} - \frac{1}{2}w)]_{x=L-c}, \tag{13}$$

where F_{ab} denotes the thrust force produced purely by the fish body due to the acceleration reaction; m_a denotes the added mass coefficient of the per unit length of the fish body:

$$m_a(x) = \frac{1}{4}\beta\rho\pi s(x)^2, \tag{14}$$

where $s(x)$ represents the local depth of the whole fish, including the body and caudal fin. $\beta(x)$ denotes the virtue mass coefficient of the fish body. ρ denotes the fluid density.

The cross section shape of the mackerel is also shown in Figure 3. The geometrical of mackerel's features were given by Videler et al. [16], and $s(x)$ can be modeled by

$$s(x) = R_1 \sin(R_2 x) + R_3(\mathrm{e}^{R_4 x} - 1)\big|_{x \leqslant x-c}. \tag{15}$$

The R_i (i=1,2$\cdots$4) constant which takes median fin geometry function of swimmer can be found in Videler's observed results [16]. We also calculate the virtue added mass coefficient $\beta(x)$ from Lighthill's calculated graph (Figure 1 in Lighthill's paper [5]) using third-order approximation with least squares fit in Matlab. Figure 4 shows the robotic fish's body mass and the virtue added mass distribution, with consideration of the dorsal and anal fins' hydrodynamic effect.

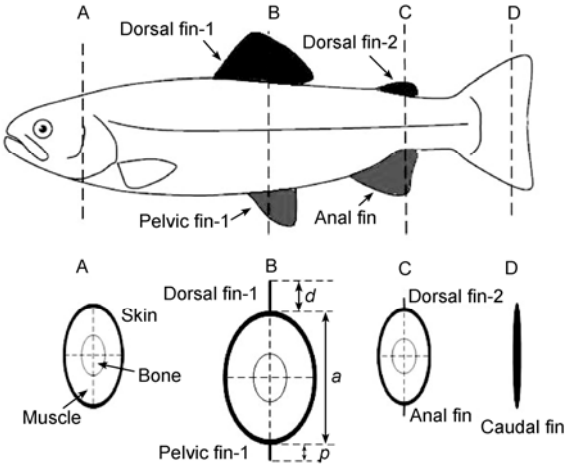

Figure 3 Schematic of anatomy of a Mackerel; images of the cross-section views are provided in A–D.

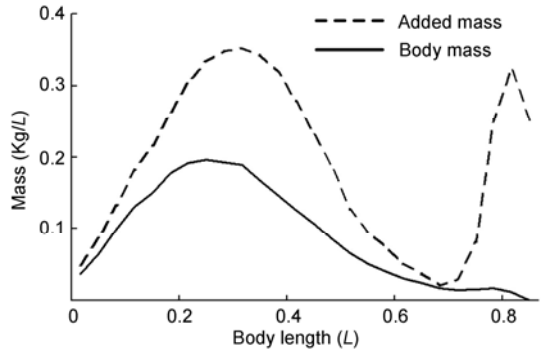

Figure 4 Distributions of fish real body mass per unit length $m(x)$ and lateral added mass per unit length $m_a(x)$.

3.4 Flapping caudal fin force

The form force acts normally on the caudal fin surface, which is denoted by F_{fc}, and can be expressed by the following:

$$F_{fc} = \frac{1}{2}\rho C_{fc} V_c^2 s_c \sin\theta, \tag{16}$$

where V_c denotes the speed of the normal component of the velocity of the tail element, and which can be denoted as

$$V_{c\perp}(x,t) = \{w(x,t)\sin[\theta(x,t)]\}_{x=L-2c/3}. \tag{17}$$

C_{fc} is the force coefficient for the form force that acts normally on the surface of a plate, and is calculated from the measurement of force that acts on a flat plate [29]. The following method is widely employed in force prediction of both aerial and aquatic oscillating animal [30]:

$$C_{fc} = C_{\text{finvisid}} - \frac{1}{1+\sqrt{Re_c}}, \tag{18}$$

where $C_{\text{finviscid}}$ denotes the form force coefficient at inviscid condition. Re_c denotes the height-specific Reynolds number of the caudal fin, which can be denoted by

$$Re_c = \left[\frac{\rho x \overline{V_{x\perp}}}{\mu}\right]_{x=L-c} = \left[\frac{\rho x}{\mu}\left(\frac{2}{\pi}\omega(c_1 x + c_2 x^2)\right)\right]_{x=L-c}, \tag{19}$$

where $\overline{V_{x\perp}} = (\frac{2}{\pi}\omega(c_1 x + c_2 x^2))$.

Therefore, $Re_c = \left[\frac{\rho x}{\mu}\left(\frac{2}{\pi}\omega(c_1 x + c_2 x^2)\right)\right]_{x=L-c}$.

The form force of oscillating tail due to inviscid effect can be denoted by

$$F_{\text{finviscid}} = \frac{1}{2}\rho C_{\text{inviscid}} V_c^2 s_c \sin\theta. \tag{20}$$

Thus (16) can be rewritten as

$$F_{fc} = F_{\text{finviscid}} - \frac{1}{2}\rho\left(\frac{1}{1+\sqrt{Re_c}}\right)V_c^2 s_c \sin\theta. \tag{21}$$

In general, $F_{\text{finviscid}}$ can be calculated by summing up two hydrodynamic effects: 1) the quasi-steady lift force due to the pitch angle; 2) the unsteady wake effect induced by the unsteady motion. We model the inviscid form force $F_{\text{finviscid}}$ of the oscillating tail by using the quasi-steady lift foil theory [31], and the inviscid lift force acting on the oscillating tail takes the following form:

$$L_c = \pi\rho cSU(t)(-\dot{h}_c + U\theta_c + \frac{1}{12}c\dot{\theta}_c) - \text{Real}(\pi\rho cSU(t)(-\dot{h}_c + U\theta_c + \frac{1}{12}c\dot{\theta}_c)(1 - Te(\frac{\sigma}{2}))), \tag{22}$$

where $\sigma = \omega c/U$ represents the reduced frequency, ω denotes the circular frequency and $\omega = 2\pi f$. Real($\cdot$) denotes taking the

real part, and $Te(\cdot)$ denotes the Theodorsen function, which is defined as

$$Te(\frac{\sigma}{2}) = \frac{K_1(\mathrm{i}\sigma/2)}{K_0(\mathrm{i}\sigma/2)+K_1(\mathrm{i}\sigma/2)} = \frac{H_1(\sigma/2)}{H_1^{(2)}(\sigma/2)+\mathrm{i}H_0^{(2)}(\sigma/2)},\ \sigma=\frac{\omega c}{U}. \quad (23)$$

The ratio of third-order polynomials was found to provide good approximation to the Theodorsen function:

$$\mathrm{Real}\left(Te\left(\frac{\sigma}{2}\right)\right) = Re\left(\frac{a_3(\mathrm{i}\sigma/2)^3+a_2(\mathrm{i}\sigma/2)^2+a_1(\mathrm{i}\sigma/2)+a_0}{(\mathrm{i}\sigma/2)^3+b_2(\mathrm{i}\sigma/2)^2+b_1(\mathrm{i}\sigma/2)+b_0}\right),\ \sigma=\frac{\omega c}{U}, \quad (24)$$

where

$$[a_3,a_2,a_1,a_0]=[0.5,1.0761,0.524855,0.045133],$$
$$[b_2,b_1,b_0]=[1.90221,0.699129,0.0455035].$$

The inviscid form force produced by the component of the caudal fin lift force acting in the axial direction along the x axis is therefore given by $F_{\mathrm{invisid}}= L_c\sin\theta\times S_c$, where S_c denotes the caudal fin area. With the above elucidation, one can obtain $F_{\mathrm{finviscid}}$. While considering the skin force of the oscillating tail, the analytical approximations for skin force that are tangential to the surface of a flat plate, the force along the x axis is expressed by the following [28, 29]:

$$F_{sc} = -\int_{L-c}^{L}(\mu(\frac{32}{\pi}V_{xc\perp}+0.32\frac{x}{s(x)}\sqrt{Re_c}V_{xc\|})\cos\theta)\mathrm{d}x, \quad (25)$$

where $v_{x\perp}=V_c=\partial h(x,t)/\partial t$ denotes the caudal fin flapping velocity normal to the body midline; and $v_{x\|}=\partial w(x,t)/\partial x$ denotes the body wave velocity tangential to the body midline. The acceleration reactive force for the caudal fin that acts in the direction along the x-axis takes the form of the following:

$$F_{ac} = \int_{L-c}^{L} C_{ac}\rho\frac{\partial w(x,t)}{\partial t}\mathrm{d}x. \quad (26)$$

The added mass coefficient of the caudal fin can be estimated by the following [5]:

$$C_{ac} = \frac{1}{4}\pi s(x)^2. \quad (27)$$

The force generated by the oscillating tail is calculated as the sum of all three types of forces, $F_c=F_{fc}+F_{sc}+F_{ac}$. The force acting on the undulating body and rigid head can be described as $F_b=F_{fb}+F_{sb}+F_{ab}$ and $F_h=F_{fh}+F_{sh}+F_{ah}$, respectively. In this paper, we treat the parts that are anterior to the caudal fin as an integrated body, the force acting on which is denoted by F_B, and $F_B= F_b+ F_h$. The Newton force balance condition in the axial direction satisfies the following:

$$F_B + F_c = m\frac{\mathrm{d}U(t)}{\mathrm{d}t}, \quad (28)$$

where m denotes the mass of robotic fish, therefore, one can solve the self-propulsive speed $U(t)$ according to eq. (28). It should be noted that the current analytical model does not capture every detail of the fluid effect, likewise, the three-dimensional shape effect was not taken into account; and the free water surface wave might also interfere with the accuracy of the experimental results. The small disparities of speed results among the simulations and experiments are possibly caused by the above-mentioned physical factors.

4 Experimental method

The computer-generated model of the robotic fish, which has a total length of 58.8 cm and 2.79 kg, shows that the robot is a relatively exact replica of a Mackerel (*Scomber scombrus*), which has two dorsal fins and two pelvic fins (i.e. the median fins), as can be seen from Figures 5(a) and

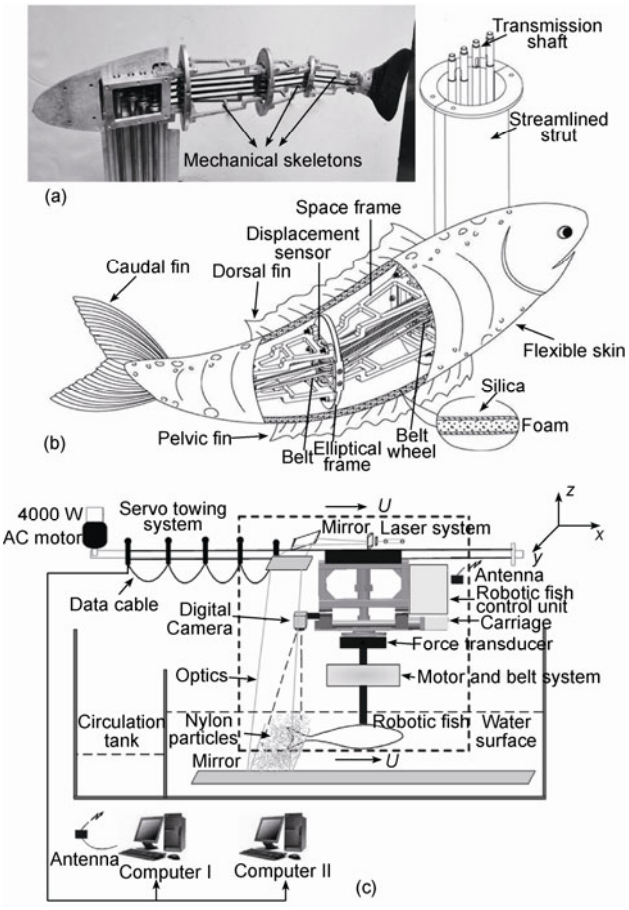

Figure 5 (a) Snapshot of the mechanical skeleton of a robotic Mackerel. (b) Actuation mechanisms for the relative rotations of the robotic links. (c) Schematic of the whole system for the self-propulsive robotic fish model, where the yellow box represents the shelf for the robotic fish power supply, motion control, amplifier and data acquisition system. The x-axis is along the fish axial length, the y-axis is in the lateral direction, and the z-axis is selected to be orthogonal to the horizontal plane.

(b). The design details of the robotic fish in the present study was previously discussed in ref. [20]. Figure 5(c) shows the schematic of the experimental setup for measuring the thrust performance of the robotic fish. The robotic fish model moves at mid-depth in the tank to avoid the interference effect of the free surface and the bottom of the tank. The external force of a robotic fish was measured using a multi-component piezoelectric force transducer Kislter 9254C. The digital particle image velocimetry (DPIV) system was used to measure the flow field generated by the robotic fish to predict the thrust force through the quantitative flow field [32]. Details of the DPIV software and open-source code can be found in ref. [33].

Conventionally, the thrust efficiency based on the thrust force for a constant swimming speed is defined by the following:

$$\eta = TU / P_{\text{fluid}}, \tag{29}$$

where U denotes the fish swimming speed, T denotes the time-averaged thrust force, and P_{fluid} denotes the time-averaged undulatory power that is purely consumed by the fluid. When the experimental apparatus was in operation we were able to simultaneously record the power consumption P_{fluid}, thrust force T and the self-propulsive speed U (denoted by U in Figure 5). Therefore, we can estimate the quantitative thrust efficiency; for more details of the experimental method please refer to our previous study [20, 34, 35].

5 Simulation and experimental results

5.1 Self-propulsive speed

First, we consider the instantaneous speed results of the three undulatory kinematics. In Figure 6, we actuated the robotic fish with three undulatory kinematics under the same oscillating frequency (f=0.8 Hz) and amplitude (h= 0.1L). The total time duration of the simulation and experiment processes were 20 s for the swimmer starting from rest to the steady swimming state, i.e., when the thrust force is balanced by drag force. Figure 6 shows both the theoretical and experimental speed results of the robotic swimmer with all three undulatory kinematics. It can be observed that the qualitative results of the simulation are consistent with the results of the experiments for all three kinematics.

As can be seen from Figures 6(a) and (b), both simulation and experimental results show that after the initial 12 beat cycles, the robotic model with all three kinetic movements achieved an averaged mean steady swimming speed. Different constant-mean speeds can be observed, and the robotic fish with carangiform and thunniform kinetic movements achieved higher velocities, with the thunniform

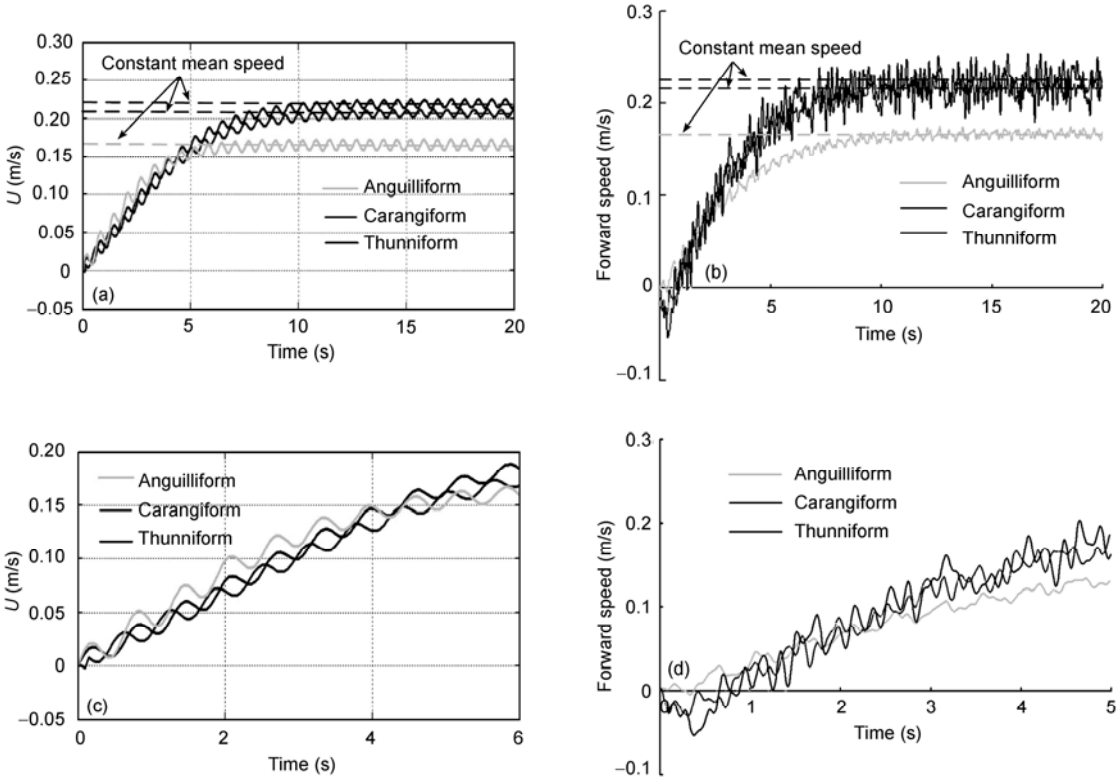

Figure 6 Speed results of the three undulatory kinematics: (a) Simulation result of swimming speed history for hybrid kinematics at f=0.8 Hz for 20 s, (b) experimental result of self-propulsive speed, (c) simulation result of speed during initial start phase and (d) experimental result of swimming speed during initial start phase.

having a slight predominance over the carangiform. A very interesting finding can be observed in Figures 6(c) and (d); during the initial acceleration phase, the robotic swimmer with the anguilliform kinetic movement accelerated faster than the other types of movement according to both experimental & simulation results. Ultimately, the swimmers with carangiform and thunniform overtook the anguilliform kinetic movement and performed better. Previous experimental studies on live fish reported that carangiform fishes, like the leopard shark and bamboo shark, frequently shorten the body wave length during some start behavior to achieve larger swimming speed [2, 21]. Current experimental results are somewhat relevant to the biological findings.

Then we consider the values of quasi-steady swimming speed. Systematic tests of both experiments and simulations at a serial of undulating frequencies ranging from 0.4 to 2.2 Hz with small increments of 0.2 Hz were performed. As shown in Figure 7, the simulation speed is linear with the undulating frequency. For all the experimental data, the self-propulsion speeds also show an approximately linear relationship with f. It should be note that a positive linear relationship between f and U is similar to the results reported for many live fish species and marine mammals [25]. In Table 1 we provide the data of the speed slope values (U/f) for all three undulatory kinematics. The largest slope value is about 0.135 for thunniform kinematics and the minimal slope is around 0.1 for anguilliform kinematics.

With regard to previous studies of live fish, we used Strouhal number (St) as a metric that can be compared with previous biological data [26]. The Stouhal number can be defined as $St=2fh/U$, where f is the flapping frequency, h is the tail end flapping amplitude, and U is the self-propulsive swimming speed. As can be seen in Table 1, the St were 0.591, 0.457, 0.433 (simulation), and 0.55, 0.43, 0.424 (experiment) for the anguilliform, carangiform, and thunniform kinematics, respectively. From the definition of St, the lower the value of the St number, the faster the robotic fish swims for a given flapping frequency and amplitude h.

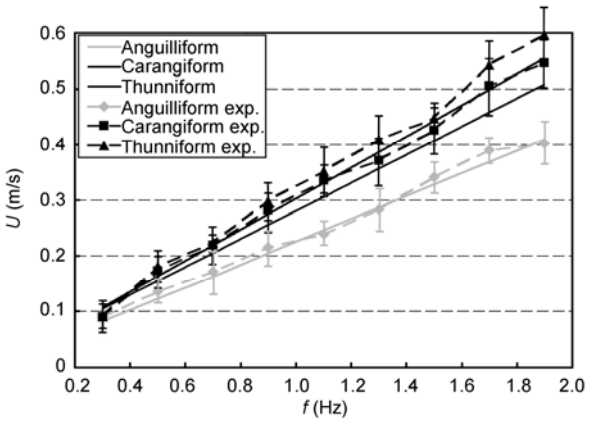

Figure 7 Self-propulsive speed vs. flapping frequency for three undulatory kinematics.

Table 1 Average steady-swimming speed and force result for three undulatory kinematics

Variable	Anguilliform	Carangiform	Thunniform
Wave length (L)	0.642	0.95	1.25
Caudal fin pitch angle (°)	26.5	20.5	11.5
Speed slope (Exp.)	0.107	0.136	0.139
Speed slope (Sim.)	0.099	0.128	0.135
St (Exp.)	0.55	0.43	0.424
St (Sim.)	0.591	0.457	0.433
Caudal fin net force (N)	0.543	0.592	0.686
Thrust force (Exp.) (N)	0.578	0.6462	0.737
Drag coefficient (Exp.)	0.059	0.039	0.038

The St obtained in the current study was higher than that achieved by most live fish in nature ($0.25<St<0.35$). This clearly reflects the disparity in swimming performance between the man-made robotic device and live fish. We speculate that one possible reason for the difference in St between the live and present robotic model is that despite various engineering innovations that have been achieved, robotic swimmers still differ from live fish in terms of skin material and body stiffness to some extent 9.

5.2 Hydrodynamic force

First, we consider the experimental force estimated from the DPIV results. Figure 8 shows the flow field generated by the robotic mackerel with all three undulatory kinematics at self-propulsive swimming speeds. In general, the large-scale characteristics of the flow pattern generated by the robotic swimmer with anguilliform and carangiform kinematics exhibit a double-row wake [36, 37]. Nevertheless, the wake structure generated by the robotic mackerel that used thunniform kinematics is different from the double-row wake but presents a typical “reverse Karman street” [26]. For the experimental force calculation method please refer to our previous study on the live fish [34]. As listed in Table 1, the experimental force by DPIV are in good agreement with the result of the theoretical model.

We then consider the disparity of instantaneous force of the three undulatory kinematics. Figures 9(a) and (b) show the instantaneous forces for the initial 3 undulatory cycles, namely the initial start acceleration phase. It can be observed that the calculated net axial force of anguilliform kinematics is superior to that of the other two kinematics. In addition, the anguilliform robotic swimmer produces the minimal drag force during the initial start. The force result may account for the acceleration advantage of the anguilliform kinematics.

The thrust force of the robotic swimmer with thunniform kinematics overtakes those of the anguilliform and carangiform kinematics during the steady swimming state, as seen in Figure 9(c). It is notable that the dimensional drag force for thunniform kinematics is the largest because the robotic swimmer with thunniform kinematics produces the maximal

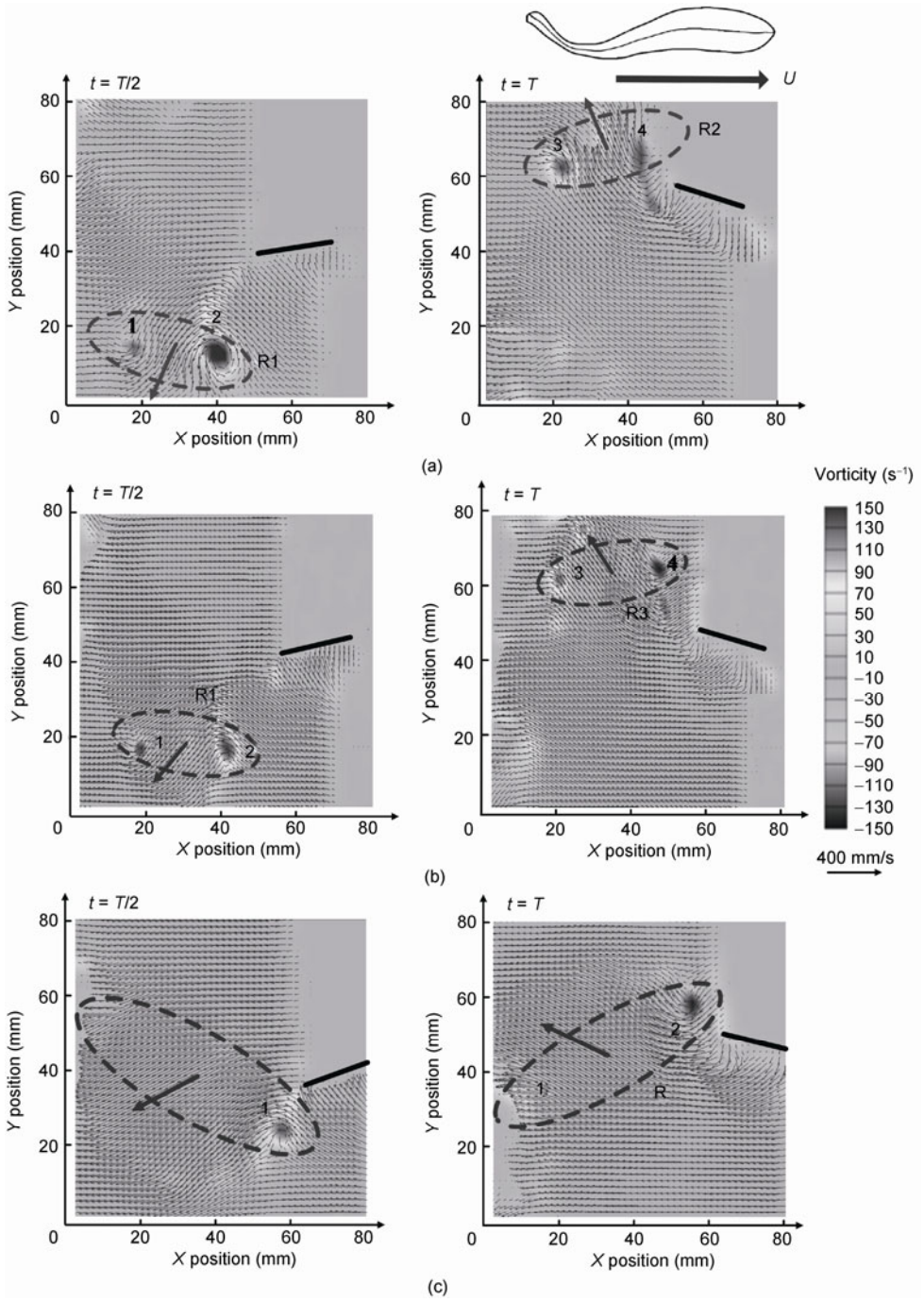

Figure 8 Flow field generated by the robotic swimmer using (a) anguilliform, (b) carangiform, and (c) thunniform kinematics, where the dark drawn lines indicate the position of the robotic fish's caudal fin.

self-propulsive speed U. Under self-propulsive condition, the thrust force T equals the drag force D, therefore the non-dimensionalized drag coefficient can be denoted as

$$C_D = \frac{D}{\rho U^2 L^2} = \frac{T}{\rho U^2 L^2}, \tag{30}$$

where ρ is the density of the fluid, U is the swimming speed of the robotic fish. The drag coefficient C_D produced by the robotic fish with thunniform kinematics was the lowest among the three kinematics. Therefore, this might be the principal reason of why thunniform kinematics is predominant in terms of steady swimming speed.

From the fluid point of view, the thrust performance results of the three undulatory kinematics can be explained by the followings. The undulatory pump mechanism (the anguilliform kinetic movement) can produce more thrusts at low swimming speed, and enables the body to push the

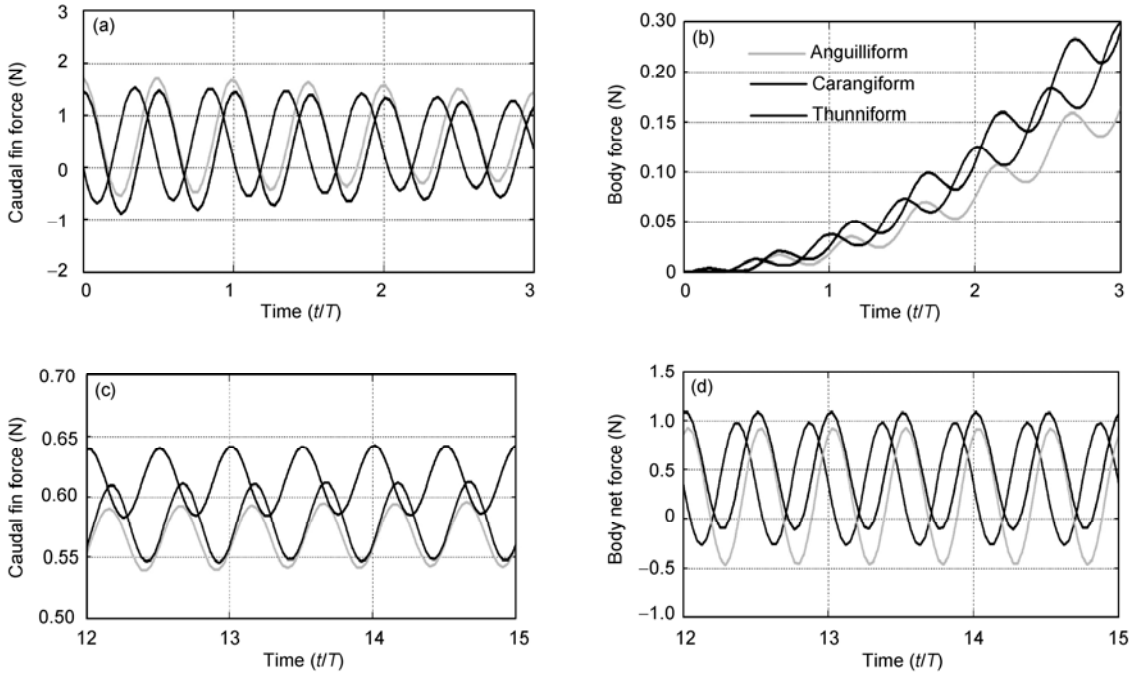

Figure 9 Body and caudal fin instantaneous forces for three undulatory kinematics. (a) Caudal fin net force during the initial 3 undulatory cycles. (b) Body net force during the initial 3 beat cycles. Note that drag force is along the axial direction towards backward, which is in the opposing direction of the thrust force. (c) Caudal fin net force in 3 undulatory cycles during steady swimming. (d) Body net force in 3 cycles during steady swimming.

water backwards more efficiently. Triantafyllou et al. [26] indicated that larger sweeping area, i.e., larger caudal fin pitch angle in the present study, is more suited for still water force generation (zero forward speed), which also clearly accounts for better start performance for anguilliform kinematics. As the speed increases, the lift-based mechanism (thunniform kinematics in the present study), which is similar to an oscillating foil, works more effectively and performs better when there is an oncoming flow speed.

5.3 Thrust efficiency

Among the existing analytical methods, thrust efficiency can only be predicted through the elongated body theory (EBT) or its improved form [5] denoted as improved EBT in the present study for simplicity, which can be expressed by eqs. (31) and (32), respectively.

$$\eta = \frac{1}{2}(1+\beta), \tag{31}$$

where $\beta = U / V_b$ and $V_b = \lambda f$. β denotes the ratio of the self-propulsive speed U of the robotic fish to the undulation wave speed V_b of the fish body. The improved EBT efficiency formula considers the slope angle effect of the fish caudal fin, and can be expressed as [38]

$$\eta = \frac{1}{2}(1+\beta) - \frac{1}{2}\gamma^2(\beta^2/1+\beta), \tag{32}$$

where $\gamma = \dfrac{\mathrm{tg}(\theta_{\max})}{h_{\max}} \times \dfrac{\lambda}{2\pi}$.

The values of pitch angle amplitude $\theta_{\max}$ for each kinematics were provided in Section 2. The quantitative results of thrust efficiency for EBT, improved EBT, and current experimental results are listed in Table 2. Although the improved EBT method takes the pitch angle hydrodynamic effect into account and is more accurate for estimating the thrust efficiency of carangiform fish such as mackerels, the improved EBT method overestimates the experimental results. Such overestimation, as discussed in recent biological and computational research papers, is largely due to the fact that both methods underestimate the total power input of fish 4. Therefore, the improved EBT method cannot obtain the actual quantitative results either. Although the deficiencies of these methods have been recognized, until now no approach has been developed yet to solve this problem. However, analytical calculations and experimental results still share the same qualitative tendency, as can be observed from Table 2. The principal findings based on Table 2 can be therefore summarized as follows: The robotic mackerel with the thunniform kinematics is the most efficient among all types of kinetic movements. The efficiency value of the robotic fish using anguilliform kinematics produces the minimal efficiency, whereas the carangiform kinematics is in between the anguilliform and thunniform kinematics both in terms of movement pattern and thrust efficiency.

Table 2 Theoretical and experimental thrust efficiency results

Variable	Anguilliform (%)	Carangiform (%)	Thunniform (%)
Experiments	26.6	31.4	47.3
EBT (Sim.)	68.4	73.1	79.2
Improved EBT (Sim.)	63.5	70.7	76.3

6 Discussions

A lot of progress has been made in understanding the fundamental mechanics of the undulatory propulsion in fishes [25, 39], but the inability to control and precisely alter individual kinematic parameters have hampered biologists' ability to understand the fundamental mechanics of the aquatic system. The mathematical modeling and robotic experiment have become increasingly essential in biomechanics recently [40, 41], offering the opportunity to focus research by creating models that can be easily controlled to move with desired kinematics in both mathematical and experimental ways.

We demonstrated that the robotic mackerel with thunniform kinematics not only reaches the highest velocity but is also most efficient during steady swimming, while the anguilliform kinematics performs better during the initial start acceleration. The present results might possibly uncover that the so-called "hybrid kinematics" has certain scientific significance for both live swimmers and biomimetic underwater robots. Documented by Sfakiotakis 1, anguilliform, carangiform and thunniform swimmers follow their own specific patterns of movement. Occasionally, however, biologists have found evidence of "hybrid kinematics" within standard undulatory locomotion patterns. The current findings suggest that the fish could achieve higher acceleration or larger thrust efficiency by changing their defined "inherent" kinematics. We speculate that this might be the reason that the "hybrid kinematics" exists in fish undulatory swimming. On the other hand, the present study might also shed light on the engineering applications; the robotic fish chooses appropriate kinematics to achieve better thrust performance, depending on situation, missions or requirements that require fast start or long-time efficient cruising. The results of the present study provide quantitative results to address this issue.

It should be point out that current findings rest on the fact that the robotic model "swims" in the controlled flow that is produced in laboratory towing tank. In the present study we only considered straight-line swimming in a uniform ambient flow environment and neglected any effects ambient vortical or turbulence. One important feature of the natural environment is that the fish occasionally swim in the turbulent flow. Previous biological results have revealed that during locomotion in freestream flows, fish exhibits the usual pattern of body undulatory movement, namely the anguilliform, carangiform and thunniform kinematics. Nevertheless, in the turbulent flow, like the Karman vortex street, fish substantially alter the pattern of body undulation that weave in between the oncoming vortices to reduce the energy consumption. This unusual locomotor behavior in large-scale turbulent flows has been termed the "Karman-gait", which is quite different from the three typical undulatory kinematics mentioned in this paper. Very little is known about how swimming fish relates to turbulence. This issue, however, was not explored in the present study and we only focus with certainty on the hydrodynamic effects of the so-called "hybrid kinematics" in the uniform flow. It is our hope that the experimental apparatus we have implemented will provide further capability of investigating fish propulsion in turbulence in the future.

7 Conclusions

In this paper, we constructed a mackerel-body-shaped robotic fish and employed it to demostrate the significance of employing a novel movement pattern-hybrid kinematics. Our main findings can be summarized as follows:

Using the self-propulsive speed as the metric, the robotic mackerel with the thunniform kinetic movement achieved a higher steady swimming speed relative to those with carangiform and anguilliform kinematics. But the mackerel using anguilliform initially performed better than the other two types of undulatory kinematics.

The theoretical instantaneous force results show that the robotic swimmer with anguilliform kinematics produces the minimal body drag and maximal thrust force during the initial start phase. However, the robotic thunniform ultimately catches up and generates lager thrust force, and smaller drag coefficient is produced during the steady swimming mode.

Considering the thrust efficiency, the thunniform undulatory kinematics is the most efficient, while the anguilliform movement produces the minimal thrust efficiency.

This work was supported by the National Natural Science Foundation of China (Grant No. 61075100). Many thanks to Prof. George V. LAUDER for the constructive suggestions on our work and sharing the fresh literatures. Also thanks was given to LI JinLan, FAN Zhe and ZHANG JingFeng for helping to conduct the experiment.

1 Sfakiotakis M, Lane D M, Davies J C. Review of fish swimming modes for aquatic locomotion. IEEE J Ocean Eng, 1999, 24: 237–252

2 Tytell E D. Do trout swim better than eels? Challenges for estimating performance based on the wake of self-propelled bodies. Exp Fluids, 2007, 43: 701–712

3 Tytell E D, Borazjani I, Sotiropoulos F, et al. Disentangling the functional roles of morphology and motion in the swimming of fish. J Exp Biol, 2010, 50: 1140–1156

4 Tytell E D, Lauder G V. The hydrodynamics of eel swimming. I.

Wake structure. J Exp Biol, 2004, 207: 1825–1841
5 Lighthill M J. Large-amplitude elongated-body theory of fish locomotion. Proc R Soc Lond B, 1971, 179: 125–138
6 Chen Z, Shatara S, Tan X B. Modeling of biomimetic robotic fish propelled by an ionic polymer-metal composite caudal fin. IEEE/ASME Trans Mechatron, 2010, 15: 448–459
7 Wen L, Wang T M, Liang J H, et al. Novel method for modeling and control investigation of efficient-swimming carangiform robotic fish. IEEE Trans Ind Electron, 2012, 59: 3176–3188
8 Wen L, Wang T M, Wu G H, et al. Hydrodynamic investigation of a self-propulsive robotic fish based on a force-feedback control method. Bioinspir Biomim, 2012, 7: 036012
9 Yu J Z, Tan M, Wang S, et al. Development of a biomimetics robotic fish and its control algorithm. IEEE Trans Sys Man Cybern Part B-Cyber, 2004, 34: 1798–1810
10 Zhou H, Hu T J, Xie H B, et al. Computational and experimental study on dynamic behavior of underwater robots propelled by bionic undulating fins. Sci China Tech Sci, 2010, 53: 2966–2971
11 Zhou C, Chao Z Q, Wang S, et al. A marsupial robotic fish team: Design, motion and cooperation. Sci China Tech Sci, 2010, 53: 2896–2904
12 Wang G, Zhang D B, Lin L X, et al. CPGs control method using a new oscillator in robotic fish. Sci China Tech Sci, 2010, 53: 2914–2919
13 Arash T, Sakineh O. A novel miniature virus-inspired swimming robot for biomedical applications. Sci China Tech Sci, 2010, 53: 2883–2895
14 Wang T M, Wen L, Liang J H, et al. Fuzzy vorticity control of a biomimetic robotic fish using a flapping lunate tail. J Bionic Engi, 2010, 7: 56–65
15 Hultmark M. Flow field measurements in the wake of a robotic lamprey. Exp Fluids, 2007, 43: 683–690
16 Hess F, Videler J J. Fast continuous swimming of Saithe (Pollachius virens): A dynamic analysis of bending moments and muscle power. J Exp Biol, 1984, 109: 229–251
17 Barrett D S, Triantafyllou M S, Yue D K P. Drag reduction in fish-like locomotion. J Fluid Mech, 1999, 392: 183–212
18 Anderson J M, Chhabra N. Maneuvering and stability performance of a robotic tuna. Integr Comp Biol, 2002, 42: 118–126
19 Dewar H, Graham J. Studies of tropical tuna swimming performance in a large water tunnel. J Exp Biol, 1994, 192:45–59
20 Wen L, Wang T M, Liang J H, et al. A novel method based on a force-feedback technique for the hydrodynamic investigation of kinematics effects on robotic fish. In Proc IEEE Conf Robot Autom, 2011. 203–208
21 Wen L, Wu G H, Liang J H, et al. Hydrodynamic experimental investigation on efficient swimming of robotic fish using self-propelled method. Int J Offshore Polar Eng, 2010, 20: 167–174
22 Peterson S D, Porfiri M, Rovardi A. A particle image velocimetry study of vibrating ionic polymer metal composites in aqueous environments. IEEE/ASME Trans Mechatron, 2009, 14: 474–483
23 Blake R W, Domenici P. Biomechanics in Animal Behavior. Oxford: BIOS Scientific, 2000
24 Donley J M, Dickson K A Swimming kinematics of juvenile kawakawa tuna (Euthynnus affinis) and chub mackerel (*Scomber japonicus*). J Exp Biol, 2000, 203: 3103–3116
25 Fish F E, Lauder G V. Passive and active flow control by swimming fishes and mammals. Annu Rev Fluid Mech, 2006, 38: 193–224
26 Triantafyllou M S, Triantafyllou G S, Yue D K P. Hydrodynamics of fishlike swimming. Ann Rev Fluid Mech, 2000, 32: 33–53
27 Gray J, Hancock G J. The propulsion of sea-urchin spermatoza. J Exp Biol, 1955, 32: 802–814
28 Hoerner S F. Fluid-Dynamic Drag. Brick Town, NJ: Hoerner Fluid Dynamics, 1965
29 Schlichting H. Boundary-Layer Theory. New York: McGraw-Hill, 1979
30 Dickinson M H. Unsteady mechanisms of force generation in aquatic and aerial locomotion. Am Zool, 1996, 36: 537–554
31 Streitlien K, Tranitafyllou G S. On thrust estimates for flapping foils. J Fluids Structures, 1998, 12: 47–55
32 Milne-Thompson L M. Theoretical Aerodynamics. New York: Macmillan. 1966
33 Mori N, Chang K. Introduction to MPIV-PIV toolbox in MATLAB-version 0.965 [EB/OL]. 2004-12-21. http://sauron.urban.eng.osaka-cu.ac.jp/~mori/softwares/mpiv
34 Wu G H, Yang Y, Zeng L J. Kinematics, hydrodynamics and energetic advantages of burst-and-coast swimming of koi carps (*Cyprinus carpio* koi). J Exp Biol, 2007, 210: 2181–2191
35 Liang J H, Wang T M, Wen L. Development of a two-joint robotic fish for real-world exploration. J Field Robotics, 2011, 28: 70–79
36 Buchholz J H, Smits A J. The wake structure and thrust performance of a rigid low-aspect-ratio pitching panel. J Fluid Mech, 2008, 603: 331–365
37 Borazjani I. On the role of form and kinematics on the hydrodynamics of self-propelled fish. J Exp Biol, 2010, 213: 89–107
38 Cheng J Y. Note on the calculation of propeller efficiency using elongated body theory. J Exp Biol, 1994, 192: 169–177
39 Liao J C, Beal D N, Lauder G V, et al. Fish exploiting vortices decrease muscle activity. Science, 2003, 302: 1566–1569
40 Chou C L, Low K H. Design and locomotion control of a biomimetic underwater vehicle with fin propulsion. IEEE/ASME Trans Mechatron, 2012, 17: 25–35
41 Hu T J, Shen L C, Lin L X, et al. Biological inspirations, kinematics modeling, mechanism design and experiments on an undulating robotic fin inspired by Gymnarchus niloticus. Mech Machine Theory, 2009, 44: 633–645